



Stratospheric impact of the Chisholm pyrocumulonimbus eruption:

1. Earth-viewing satellite perspective

M. Fromm,¹ O. Torres,^{2,3} D. Diner,⁴ D. Lindsey,⁵ B. Vant Hull,⁶ R. Servranckx,⁷
E. P. Shettle,¹ and Z. Li⁸

Received 6 July 2007; revised 30 November 2007; accepted 7 January 2008; published 17 April 2008.

[1] The pyrocumulonimbus storm near Chisholm, Alberta, on 28 May 2001 has been studied in depth. However, the impact of this eruption on the lower stratosphere has not been characterized. Here and in a companion paper we explore this topic. This paper focuses on the “young” Chisholm smoke plume, from the age of ~ 3 h to 1 week, as observed by Earth-viewing satellite instruments. (The companion paper presents strictly profile data.) GOES visible and infrared image loops reveal the pyroconvective life cycle and initial transport of the smoke cloud. MISR stereographic heights are the first of their kind for a stratospheric cloud, showing smoke up to 5 km above the tropopause on 29 May. MODIS IR and visible images are analyzed to give constraints on plume height, thickness, and particle size. Infrared brightness temperature analyses reveal unique aspects of the “day-after” Chisholm plume. Particle sizes are 1/3 to 1/2 compared to normal cirrus crystals. The daytime 29 May plume is optically thick at tropopause temperatures yet smoky brown. A transition from deep anvil blow off to “dry” smoke is still occurring after ~ 1.5 d. TOMS aerosol index is used as a proxy for areas of particularly high smoke plume altitude. The Chisholm smoke in the upper troposphere and lower stratosphere is traced with AI for 1 week as the plume blows across North America to western Europe. First estimates are made of stratospheric smoke mass in relation to emissions during pyroconvection. The 29 May stratospheric Chisholm pyroCb plume contains a mass between $\sim 1.39 \times 10^4$ and 1.09×10^5 t. This represents between $\sim 10\%$ and 121% of total particle mass emitted from the fire on 28 May, calling into question some frequently assumed values for smoke single scatter albedo and/or emission estimates. Strictly in terms of mass, the stratospheric Chisholm plume amounted to $\sim 15\%$ of background Northern Hemispheric stratospheric sulfate aerosol. Overall, the young pyroCb plume is seen to be a peculiar mixture of smoke aerosols and water-ice that confounds operational cloud/aerosol detection routines and exhibits extreme, and still mysterious, composition and life cycle features.

Citation: Fromm, M., O. Torres, D. Diner, D. Lindsey, B. Vant Hull, R. Servranckx, E. P. Shettle, and Z. Li (2008), Stratospheric impact of the Chisholm pyrocumulonimbus eruption: 1. Earth-viewing satellite perspective, *J. Geophys. Res.*, *113*, D08202, doi:10.1029/2007JD009153.

1. Introduction

[2] Smoke and other biomass burning emissions in the lower stratosphere (LS) have been observed and documented on at least nine occasions, in 1950 [Penndorf, 1953], 1992 [Livesey et al., 2004], 1994 [Waibel et al., 1999], two events in 1998 [Fromm et al., 2000, 2005; Siebert et al., 2000], 2001 [Fromm and Servranckx, 2003] (hereinafter referred to as FS03), 2002 [Jost et al., 2004],

2003 [Fromm et al., 2006], and 2004 [Damoah et al., 2006]. In all except the earliest case the cause was either identified as or speculated to be large forest or bush fires involving deep pyroconvection. (The source in the Penndorf case was a large Canadian forest fire but convection was not identified or suspected.) The most extreme manifestation of pyrocumulonimbus, now being called pyrocumulonimbus (pyroCb for short), is a fire-aided or fire-caused severe convective storm that reaches the upper troposphere, lower

¹Naval Research Laboratory, Washington, D. C., USA.

²NASA Goddard Space Flight Center, Greenbelt, Maryland, USA.

³Joint Center for Earth Systems Technology, University of Maryland, Baltimore County, Greenbelt, Maryland, USA.

⁴Jet Propulsion Laboratory, Pasadena, California, USA.

⁵Regional and Mesoscale Meteorology Branch, National Environmental Satellite, Data, and Information Service, NOAA, Fort Collins, Colorado, USA.

⁶Cooperative Remote Sensing Science and Technology Center, NOAA, City College of New York, New York, USA.

⁷Canadian Meteorological Center, Dorval, Quebec, Canada.

⁸Earth System Science Interdisciplinary Center, University of Maryland, College Park, Maryland, USA.

stratosphere (UTLS), involves lightning, precipitation and/or hail, extreme winds, and in some cases even tornadoes [Fromm *et al.*, 2006]. The role and importance of intense pyroCb in transporting smoke and other biomass burning emissions into the UTLS are still in the early stages of our understanding. Presently, the various aspects of this phenomenon are still incompletely characterized, but new observations, surveys, and simulations of the pyroCb are on the increase.

[3] It has been established that pyroCb can produce a twofold to fivefold increase in zonal average lowermost stratospheric aerosol optical depth [Fromm *et al.*, 2000, 2005, 2006]. Certain aspects of the pyroCb combustion/convection dynamic that enable the production and transport of such aerosol abundances into the LS are now being explored. For instance, the Fromm *et al.* [2006] case study of a pyroCb in Canberra Australia (aided by radar, photographs, and photogrammetric ground damage assessment) found that the firestorm manifested unique cloud microphysics, spawned a tornado, and had plume characteristics consistent with a volcanic eruption [Tupper *et al.*, 2005]. Another case for which the details are being intensely studied is the Chisholm fire (Alberta, Canada, 55°N, 114°W) and pyroCb of 28 May 2001 (FS03). Several additional investigations of the Chisholm pyroCb have since been initiated because of the wealth of untapped data [e.g., Rosenfeld *et al.*, 2007] (hereinafter referred to as R07) and a motivation to simulate the Chisholm pyroconvection [Trentmann *et al.*, 2006; Luderer *et al.*, 2006] and smoke plume heating/lofting [Stenchikov *et al.*, 2006].

[4] One area of uncertainty regarding extreme pyroconvection is the immediate postconvection plume. A quantitative understanding of the pyroCb injection is necessary for characterizing the eruption energetics, fuel consumption, and reconciling this “initial condition” of a UTLS plume with downstream impact. Works such as FS03 and Fromm *et al.* [2005] documented peculiar and suggestive qualities of the “day-after pyroCb” plume observed from satellite. In summary, what was seen is a mesoscale cloud that is gray or smoky in color, opaque in the thermal infrared (TIR) at brightness temperature (BT) representative of the tropopause region, and having an ultraviolet backscattering aerosol index (AI) of extremely large positive values [Fromm *et al.*, 2005]. In this paper we explore in detail the Chisholm pyroCb “day-after” plume and the evolution of this plume in the week after the injection into the LS. The present work is motivated by revelations since FS03 that provide objective constraints on parameters such as the young plume’s altitude. Moreover, the Total Ozone Mapping Spectrometer (TOMS) retrieval algorithm graduated to version 8 [Bhartia, 2007] since FS03, resulting in enhanced sensitivity of the AI to UTLS aerosols. This is a companion paper to Fromm *et al.* [2008], which deals with profile views of the Chisholm plume. These include several solar occultation instruments (POAM III, SAGE II, and HALOE), as well as from seven lidar sites ranging from Ny Ålesund, Norway to Mauna Loa, Hawaii, and balloon-borne optical particle counter measurements from Laramie, Wyoming. They show that the smoke covered most of the Northern Hemisphere, and produced localized heating of the stratosphere in the smoke layers.

[5] In this work we integrate several Earth-viewing satellite imager views of the Chisholm UTLS smoke plume in the first week after the pyroCb. The primary aim is to establish, to the extent possible, quantitative constraints on the young plume’s UTLS altitude, geometric thickness, smoke particle abundance and size. A second aim is to characterize the physical evolution of the plume in the first week after the injection. The satellite instruments consist of the Moderate Resolution Imaging Spectrometer (MODIS) [King *et al.*, 1992; Kaufman *et al.*, 1997] and Multiangle Imaging Spectroradiometer (MISR) [Diner *et al.*, 1998] aboard the Terra platform, Earth Probe TOMS [Torres *et al.*, 2002a], and the Geostationary Operational Environmental Satellite (GOES).

[6] In section 2 we describe the data sets used. Section 3 contains an analysis of the “day-after” Chisholm plume as observed by GOES, TOMS, MODIS, and MISR. In section 4 we compare MODIS and TOMS views of the Chisholm plume on 30 May 2001 with the 29 May “day-after” plume. Section 5 contains the analysis of the movement of the plume in its first week revealed by TOMS AI maps. Discussion and summary are contained in section 6.

2. Data Sets

2.1. MISR

[7] MISR provides continuous multiangle imagery of the sunlit Earth. The instrument contains nine charge-coupled-device-based pushbroom cameras to observe the Earth at nine discrete view angles: One view points toward nadir, and the other eight are symmetrical views at 26°, 46°, 60°, and 70° forward and backward of nadir. Images at each angle are obtained in four spectral bands centered at 446, 558, 672, and 866 nm. The swath width of the MISR imaging data is 400 km. It takes 7 min for any particular scene to be observed at all nine viewing angles. In its global observing mode, data from the red band of all of MISR’s off-nadir cameras, and in the four bands of the nadir camera, are acquired at 275-m spatial resolution; all other channels are averaged on board to 1.1-km resolution to conserve data rate. See Diner *et al.* [1998] for more details.

[8] Ground data processing maps MISR radiances to a Space Oblique Mercator projection, which geolocates and coregisters the data from all instrument channels to both the WGS84 (World Geodetic System Earth reference frame revised in 1984) ellipsoid and to the surface terrain altitude. Geolocation uncertainty is estimated to be ± 50 m, and coregistration errors are < 1 pixel (275 m). Ongoing assessments of image geolocation and coregistration are performed to ensure product quality [Jovanovic *et al.*, 2002, 2007]. The high-resolution, ellipsoid-projected red-band radiances are operationally used in an automated algorithm to derive cloud top and aerosol plume top heights relative to the surface. Pattern matching is used to determine the geometric parallax (horizontal displacement) for elevated atmospheric features, and stereo-photogrammetric algorithms transform these parallaxes into cloud top or plume top heights [Moroney *et al.*, 2002; Muller *et al.*, 2002; Zong *et al.*, 2002]. In the standard MISR Level 2 Stereo Product, which uses the nadir and 26° cameras in the height retrievals, the quantized precision of the resulting height field is ± 560 m. Altitudes for clouds as well as smoke and dust

plumes are routinely retrieved and reported on a 1.1-km resolution geolocated grid. Because the heights are derived geometrically, they are insensitive to atmospheric temperature profile, emissivity, and absolute radiometric calibration uncertainties. Validation using ground-based 35/94 GHz radar and lidar retrievals of single-layer clouds shows instantaneous accuracies typically in the 500 m–1 km range [Naud *et al.*, 2002, 2004, 2005a, 2005b; Marchand *et al.*, 2007]. Since the technique is purely geometric, comparable accuracy is expected for aerosol layers.

[9] Owing to the 7-min interval from when MISR first sees a scene with the forward 70° camera to its last view with the backward 70° camera, the motion of clouds or aerosols during this time contributes to the disparity between image pairs and therefore must be distinguished from the parallax due to height. Consequently, a “wind correction” should in general be applied to the derived stereoscopic heights. This can be derived from a triplet of views (nadir, 46°, and 70°) [Horváth and Davies, 2001; Zong *et al.*, 2002]. Only the along-track component of motion contributes to the uncorrected parallax error. The magnitudes of wind corrections are typically <1 km in height. Given the better density of coverage typically obtained with the non-wind-corrected heights, and the generally small height error associated with winds, it is often more convenient to ignore the wind corrections when the resulting uncertainty is tolerable.

[10] Many aerosol plumes are too tenuous to be reliably detected in the nadir and 26° views which are used in MISR’s operational height retrievals. However, the MISR 60° and 70° views are much more sensitive to thin plumes because of the oblique slant path. Specialized runs of the MISR stereo retrieval algorithm demonstrate that it works well with the oblique cameras and improves the height coverage for thin clouds, elevated aerosol layers, and near-surface plumes that the operational product currently misses.

2.2. TOMS Aerosol Index

[11] The TOMS sensor detects UV absorbing aerosols with the well known AI parameter [Herman *et al.*, 1997]. The AI is a measure of the spectral contrast change in the UV (331 and 360 nm) resulting from the presence in the atmosphere of light absorbing particles. Thus, the AI is primarily a measure of the “missing” Rayleigh-scattered (and cloud-reflected) radiation at the top of the atmosphere that has been absorbed by the aerosols. The AI magnitude depends strongly on the aerosol layer height above the ground and its optical depth [Torres *et al.*, 1998]. The sensitivity of AI to aerosol layer height can be advantageously used for the unambiguous detection of UTLS absorbing aerosol layers generated by pyroconvection. These highly elevated aerosol layers yield unusually high AI values (10 or larger) clearly associated with their UTLS location. Aerosol Index values for large tropospheric aerosol loads associated with biomass burning or desert dust aerosols are typically no larger than about 8. The ability to detect UTLS absorbing aerosols is a clear improvement of the TOMS version 8 data [Bhartia, 2007]. In version 7 the AI data was artificially truncated at a value of 12.8. By removing this arbitrary limit the TOMS aerosol data has

become a very useful tool for the detection and tracking of pyroconvection activity [Fromm *et al.*, 2005].

2.3. MODIS

[12] We use Terra MODIS collection 5 level 1b data [Yang *et al.*, 2007, and references therein]. Our analysis uses 1 km resolution data from visible channels 1 (0.645 μm), 3 (0.469 μm), and 4 (0.555 μm) for true-color imagery and radiance data from the THIR channels 31 and 32 (11 and 12 μm), expressed as brightness temperature. In addition to the level 1b data, we also exploit MODIS level 2 aerosol [Remer *et al.*, 2005] and cloud [King *et al.*, 1992, 2003] products.

3. Chisholm “Day-After” Smoke Plume: 29 May 2001

[13] The Chisholm fire erupted into pyroconvection in the late afternoon on 28 May 2001, at approximately 0000 UTC 29 May (FS03). The active convection persisted for about 3 h and created an opaque smoke/ice anvil with 11 μm brightness temperatures lower than -60°C , $\sim 2^{\circ}\text{C}$ lower than the tropopause temperature (R07). After 0300 UTC the pyroconvection ceased and the residual plume, spanning the tropopause into the lowermost stratosphere, moved north toward the Northwest Territories (NWT).

[14] The evolution from pre-pyroCb to residual plume was captured with a day-long animation of GOES imagery, for the period 2200 UTC 28 May to 2345 UTC 29 May (Animations 1 and 2).¹ Animation 1 shows visible (during daylight) and shortwave IR (3.9 μm) during nighttime. The visible frames contain 3.9 μm hot spot pixels. The animation shows the apparently expanding/heating Chisholm fire, the pyroCb pulsing in two main phases, and the expansive cold/opaque cloud persisting through the night. Animation 2 is a THIR animation. The THIR animation is summarized by a time series in Figure 1, which shows the transformation of the peculiarly and persistently cold Chisholm plume. After cessation of pyroconvection the plume continued to emit at BT $< -60^{\circ}\text{C}$ for ~ 13 h, well after sunrise 29 May. Surrounding radiosonde observations at 1200 UTC all record temperature minima greater than that of the plume top. Moreover, the area with BT $< -60^{\circ}\text{C}$ expanded throughout the night and into daylight, to roughly 46000 km² 8 h after pyroconvection. THIR cooling in time of an individual tropospheric cloud would normally be interpreted as a thickening and/or rising thick cloud. We do not have a satisfactory explanation for this cooling of a postconvection cloud top. However, we have observed it in other pyroCb cases (not shown), yet not for “regular” convection.

[15] After sunrise on 29 May the plume is a large, smooth gray cloud that spreads and arcs through NWT and then southeastward toward Hudson Bay. Next we will analyze the post-pyroCb plume with polar-orbiting satellite views at two times during this “day after.”

3.1. Nighttime MODIS View

[16] Here we introduce MODIS THIR image data to gain insights into the Chisholm plume’s height, opacity, and plume particle size. The wealth of IR channels provided

¹Animation 1 is available in the HTML.

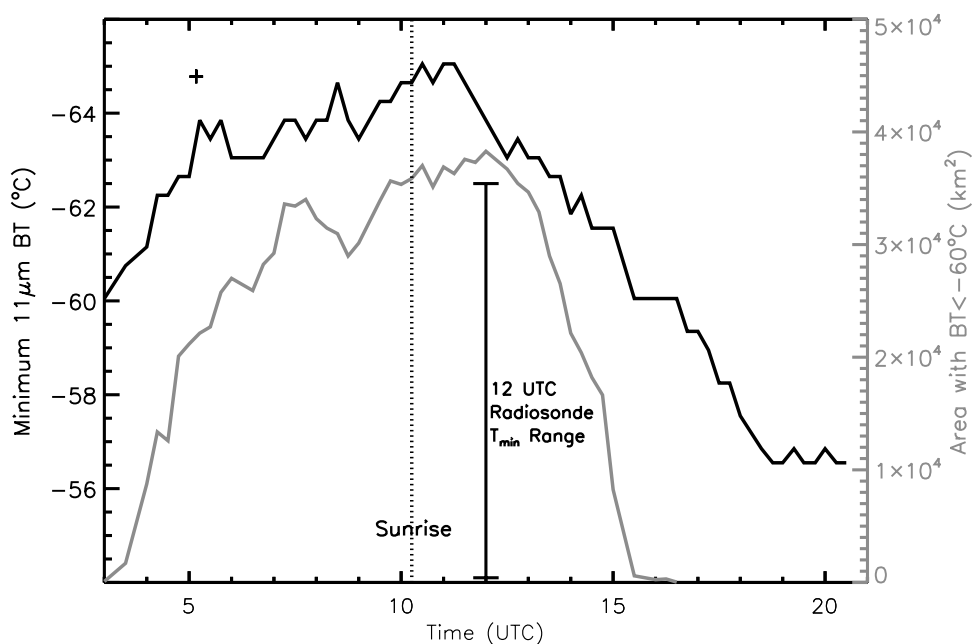


Figure 1. Timeline of GOES 11 μm BT minimum (black) and pixel area (gray) for pixels with BT $< -60^\circ\text{C}$ following the Chisholm smoke plume between 0300 and 2100 UTC 29 May 2001. Vertical bar gives range of 1200 UTC radiosonde T_{min} for four closest and surrounding launch sites: Fort Smith (60°N , 112°W), Fort Nelson (59°N , 123°W), Norman Wells, (65°N , 127°W), and Cambridge Bay (69°N , 105°W). Sunrise time at vertical dotted line. MODIS 0510 UTC BT minimum, plus symbol.

by MODIS is quite valuable; here we focus on two THIR wavelengths (11 and 12 μm) that have been successfully used on clouds and volcanic plumes, and which are common among the operational geostationary and polar orbiting imagers. We use a THIR BT difference technique that gives information on cloud particle physical properties in darkness and daylight.

[17] The 29 May Terra MODIS nighttime IR imagery (0510 UTC, 2210 LST) captures the young plume about 3 h after pyroconvection collapsed. Figure 2a gives the THIR BT. The Chisholm plume has a substantial area colder than -60°C . As R07 reported, this represents an optically opaque surface above the local tropopause. It is obvious from the low BT that the young Chisholm pyroCb plume is distinctive from all the other clouds in this scene, even though deep nonpyroconvection occurred the prior evening (R07). Note that the MODIS 0510 UTC BT minimum is even lower than the GOES value at that time (shown in Figure 1).

[18] Figure 2b contains a brightness temperature difference (BTD) image. BTD is defined as 11 μm BT minus 12 μm BT. This so-called “split-window” technique has been used to evaluate volcanic cloud composition [e.g., Wen and Rose, 1994] and meteorological cloud particle size [Gothe and Grassl, 1993]. Split-window BTD is expected to be zero to slightly positive (i.e., generally $< +1.0$ K) for optically thick water-ice clouds. However, for high-altitude optically thin meteorological or volcanic cloud, BTD departs considerably from zero. Thin water-ice clouds over a warmer surface typically give a positive BTD [Yamanouchi et al., 1987]; ash-rich optically thin volcanic clouds may have the reverse effect, leading to negative BTD [Prata, 1989]. BTD has been used effectively as a detection

method for yet another peculiar cloud form, the ice-rich high-tropospheric volcanic plume [e.g., Rose et al., 1995, 2003]. The implication in such cases is that large positive BTD signifies anomalously small ice crystals populating a plume dominated by ice and ice-coated ash. In the present case of the 0510 UTC Chisholm pyroCb blow-off, BTD is near zero in the innermost portions of both residual anvils (where THIR BT is quite cold), and strongly positive on the perimeter, especially the eastward side. In this zone the cloud edge overlies cloudless skies (note the adjacent “warm” THIR BT in Figure 2a). The BTD here approaches $+10^\circ\text{C}$, much larger than anywhere else in the MODIS scene.

[19] According to the radiative transfer modeling framework in the work by Guo et al. [2004, Figure 4a], BTD in this range is reserved for a population of cloud particles with exceptionally small effective radius compared to typical cirrus ice crystals. Prata and Barton [1993] used both a radiative transfer model and satellite THIR observations to demonstrate the relation of BTD to 11 μm BT for a range of cloud optical depth and ice crystal effective radius. Prata and Barton [1993, Figure 6] show that BTD is near zero for clear sky (warm THIR) and optically thick, cold ice clouds, and increasingly positive in between. The positive departure from zero at a given optical depth or BT increases with decreasing particle size. Maximum BTD for cirrus cloud with nominal effective radius (~ 30 μm) is $\sim +3\text{K}$ in simulation and observation [Prata and Barton, 1993, Figure 14].

[20] We replicate that type of analysis with the 0510 UTC MODIS data in Figure 3, BTD as a function of 11 μm BT. Three color-coded samples were taken from separate scenes (shown in Figure 2) sampling Phase I and II Chisholm plume segments and meteorological cloud. Each scene

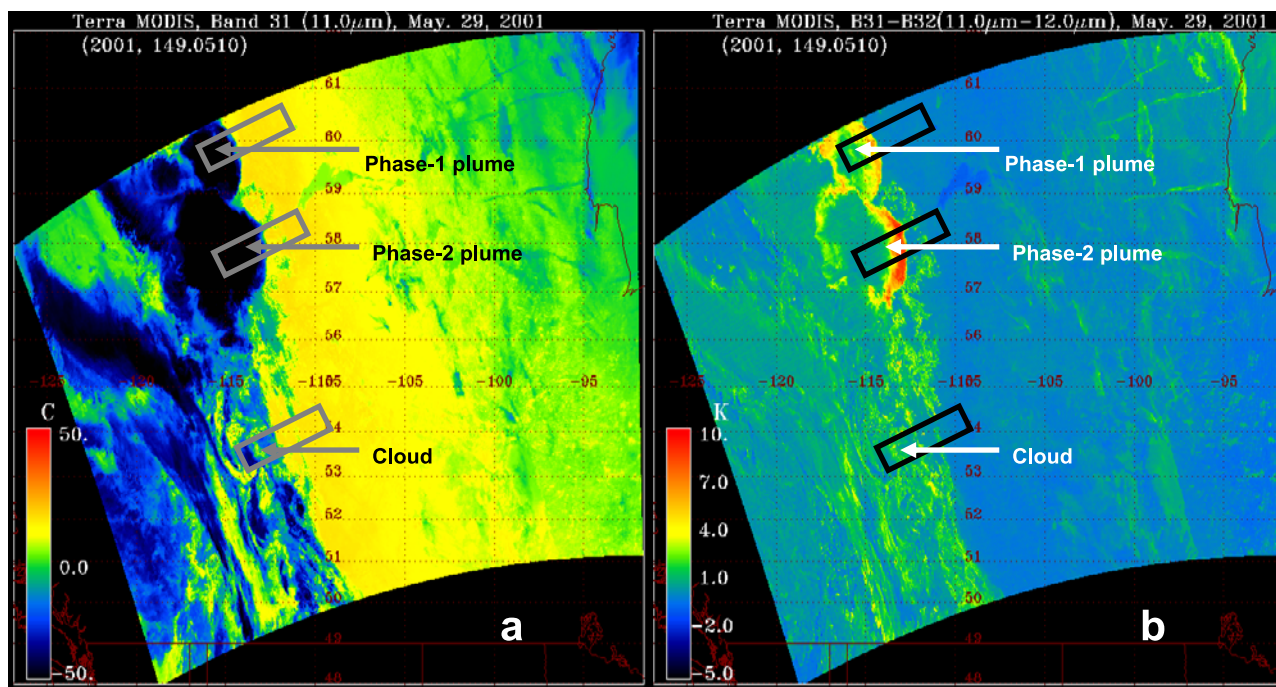


Figure 2. (a) Terra MODIS nighttime 11 μm brightness temperature (BT) imagery at 0510 UTC 29 May 2001. Boxes show scenes for which a BTD analysis is performed. (b) Terra MODIS 11–12 μm brightness temperature difference (BTD) imagery at 0510 UTC 29 May 2001. Boxes show scenes for which a BTD analysis is performed.

spans between cloud core and clear air to the east. Also in Figure 3 are curves from a radiative transfer model assuming spherical ice particles [Prata and Grant, 2001], showing BTD versus BT for three values of effective radius. Like the simulation and observations of Prata and Barton [1993], the BTD at the warm (clear air) and cold (optically thick cloud) extremes of each scene cluster near BTD = 0°C. The otherwise most obvious feature in Figure 3 is the arcing BTD in between these limits for the Phase I and II plume segments, reaching a maximum of roughly +6°C and +9°C, respectively. These arcs conform well to theoretical arcs for ice particles of 16 and 12 μm , respectively. The plume arcs are distinctive in comparison to the BTD pattern for the meteorological cloud, the core of which is cold enough (<−40°C) to indicate ice. The conforming theoretical effective radius for the cloud/plume pixels at BT = −40°C suggests that the plume segments are distinctive from one another (in terms of effective radius), yet both are distinctive from a nearby cold meteorological cloud. In this first application of the BTD versus BT analysis to a smoke plume we make no claim in terms of absolute value of the particle effective radius, but rather conclude that such a young, deep, optically thick smoke plume is characterized by particles smaller by a factor of 2–3 compared to average meteorological cloud ice. Interestingly though, the 0510 UTC plume top effective radius (~10–15 μm) is quite similar to the retrieved effective radius for the Chisholm pyroCb reported by R07.

[21] We will perform the BTD analysis again for the daytime 29 May MODIS view of the Chisholm plume, discussed next. However, here we refer the reader to the auxiliary material section for a BTD analysis of the active

pyroconvective phase of the Chisholm fire discussed in great detail by R07.² The BTD pattern during active pyroconvection (~0200 UTC) is quite consistent with the postconvection plume at 0510 UTC.

3.2. Daytime 29 May Views

3.2.1. MODIS Visible

[22] Daytime (1840 UTC; 1140 LST) 29 May Terra MODIS views of the “day-after” Chisholm plume are shown in Figure 4. A stretched true-color rendering in Figure 4a illustrates the breadth and abundance of smoke. Along the west, north, and east perimeter the smoke overlies pure white water-ice cloud, with weak yet discernable shadowing suggesting higher smoke altitude. To the south a tongue of smoke is translucent over cloud-free sky. The perimeter smoke is relatively gray and smooth, and becomes dark brown and textured toward the core.

3.2.2. MODIS THIR

[23] Figure 4b shows the THIR image. Much of the smoke plume core is opaque at BT < −40°C, which is a proxy for upper tropospheric altitude and represents a condition assuring homogeneous freezing [Wallace and Hobbs, 1977]. Thus any conventional cloud particles inside this contour would be in the form of ice. We see by comparison with the nighttime view in Figure 2a that the general cloud top BT has increased but is still quite low within the smoke plume, and lower than anywhere else in the image. Considering the spatial correspondence of low BT and smoky color, and the likelihood that this correspon-

²Auxiliary materials are available in the HTML. doi:10.1029/2007JD009153.

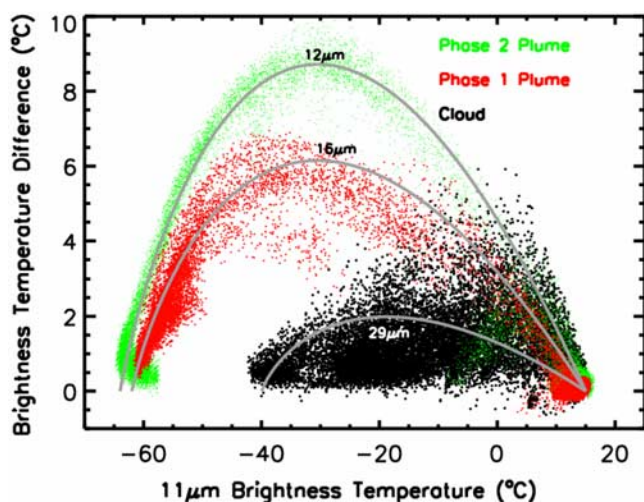


Figure 3. MODIS split-window BT analysis, 0510 29 May 2001. Independent variable is $11 \mu\text{m}$ BT ($^{\circ}\text{C}$); dependent variable is $11\text{--}12 \mu\text{m}$ BT. Target scenes are color coded and labeled on the figure. Gray lines are theoretical curves from a radiative transfer model (see text for details) for ice cloud particles of the labeled effective radius.

dence also applied during the overnight observation, we conclude from this plume top “warming” that an evolutionary drying out of the smoke plume is taking place. That is, smoke-polluted ice is sublimating, thereby transitioning to smaller crystals and “dry” smoke. It is worth noting again that the Chisholm plume’s BT is still distinctively low compared with other clouds in this scene, and that there is no clear evidence of other convective blow off from the prior evening’s “regular” convection. Hence the smoke-ice pyroCb plume appears to be a particularly persistent form of anvil blow off compared with “regular” Cb blow off.

3.2.3. MODIS BT

[24] The BT at 1840 UTC is shown in Figure 4c. Here again the Chisholm plume has a distinctive signature, generally large BT, albeit transformed from the nighttime view $1/2$ d earlier. Here the area with the generally smoky color

(Figure 4a) is notably positive in BT; however, the maximum BT is depressed in comparison to the nighttime view.

[25] A BT analysis like that of section 3.1 and the auxiliary material is shown in Figures 5 and 6. Figure 5 gives the true-color and THIR images with boxes showing where the BT analysis is performed. We chose an exclusively meteorological cloud subsense (A), the plume and surrounding cloudy/clear area (B), and the core of the cold smoke plume (C). The BT for A (Figure 6) is uniformly close to zero, from clear-sky through thick/cold cloud BT. For guidance and comparison, the vertical bar at $\text{BT} \sim -40^{\circ}\text{C}$ is placed to isolate the coldest cloud tops. The plume BT not as large as at 0510 UTC. However, it is positively offset from $\text{BT} = 0$ compared to the meteorological clouds at $\text{BT} < -40^{\circ}\text{C}$, even in the inner core (i.e., optically thickest section) of the plume.

[26] To our knowledge this peculiar condition is not documented in the literature. The BT signature at 1840 UTC indicates that the plume top composition and/or prevailing particle size is unique, a conclusion reinforced by the strong smoky coloration. Thus it appears that deep, optically thick “day-after” pyroCb plumes can create a uniquely positive BT signature in sunlit conditions. It would be valuable in future work to study other similar plumes from both an observational and radiative transfer modeling standpoint.

3.2.4. MODIS Aerosol and Cloud Product

[27] The GOES and MODIS visible and IR data shown so far have revealed several strong peculiarities in the Chisholm smoke plume, both with respect to “normal” smoke and meteorological cloud. That impression is reinforced in the MODIS level 2 aerosol and cloud products for the 1840 UTC scene. Figure 7a gives a composite of true-color with aerosol optical depth (AOD); Figure 7b shows cloud top pressure (CTP) with AOD. The true-color/AOD composite reveals that the MODIS aerosol retrieval delivered results only for the fringe of the plume around what is labeled “dry” smoke (a characterization based on the transparency of the plume there in the THIR (see Figure 4b), and its apparent extension beyond the large water-ice cloud deck). This portion of the overall smoke plume was what the MISR footprint revealed to be low-mid-tropospheric smoke. Notice the gradient in AOD toward the

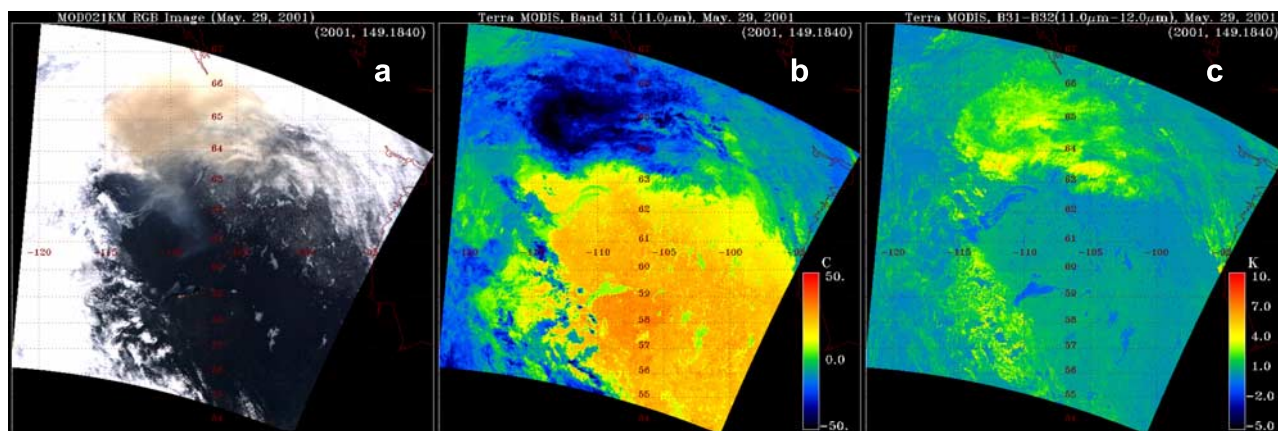


Figure 4. (a) MODIS stretched true-color image at 1840 UTC 29 May 2001. (b) MODIS $11 \mu\text{m}$ BT image at 1840 UTC 29 May 2001. (c) MODIS $11\text{--}12 \mu\text{m}$ BT image at 1840 UTC 29 May 2001.

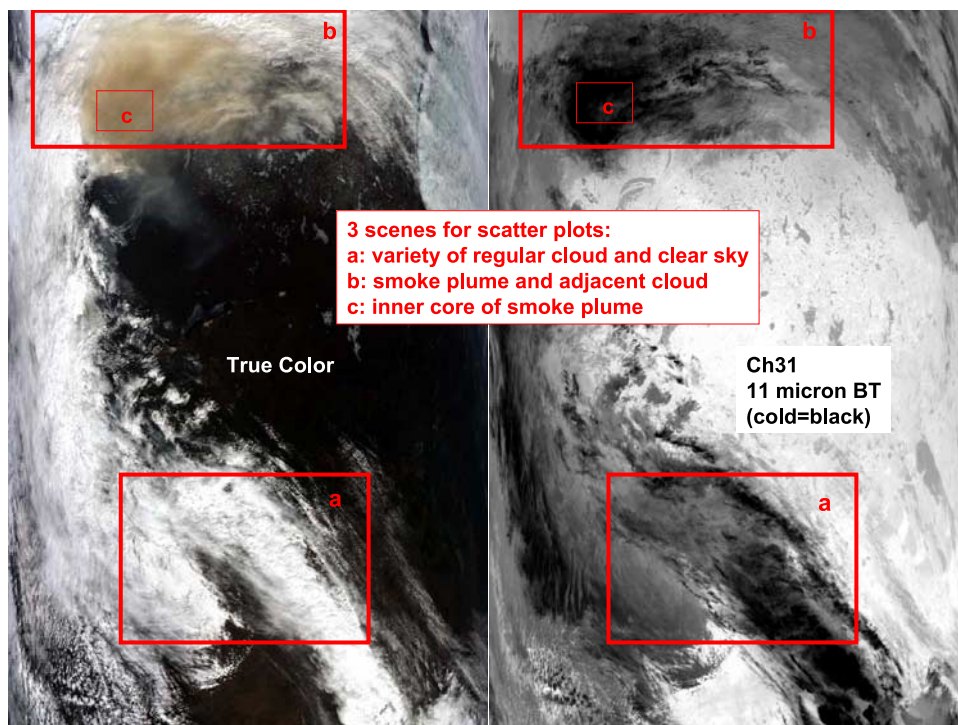


Figure 5. MODIS true-color and 11 μm BT at 1840 UTC 29 May, with boxes discriminating three scenes for split-window BT analysis. Scene a contains only meteorological cloud. Scene b contains the smoke plume and surrounding meteorological cloud. Scene c is restricted to the smoky core of the plume.

visible thicker smoke; AOD values peaked here between 2.0 and 3.0. The CTP/AOD composite in Figure 7b reveals the reason for the aerosol retrieval boundary: the majority of the plume was identified as cloud. Not shown, but worth noting, the MODIS cloud optical depth map showed the plume to have cloud optical depth values at the lowest CTP (i.e., highest altitude) significantly smaller than for the adjacent water-ice clouds, generally by a factor of 5. Thus the peculiar, combined visible and IR signals from the young Chisholm plume confounded the operational MODIS cloud and aerosol

retrievals. It may be instructive though to note that the MODIS visible AOD at the fringe of the plume was strongly increasing and peaking at values ~ 3 , suggesting that the true visible AOD of the plume core was much greater.

3.2.5. MISR

[28] The eastern portion of the Chisholm plume sampled by MODIS was simultaneously sampled by MISR also on the Terra satellite (Figure 8). The natural color view is from the MISR 60° forward viewing camera. A pall of yellowish smoke is apparent both above the surface and clouds. The

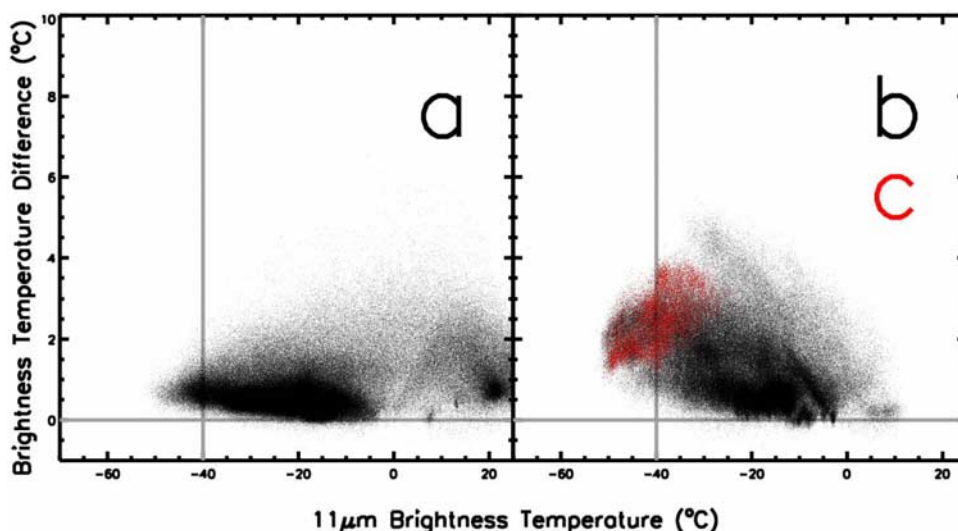


Figure 6. BT analysis for 1840 UTC 29 May. Abscissa and ordinate ranges are identical to 0510 UTC analysis in Figure 2. (left) Scene a of Figure 4. (right) Both scenes b (black dots) and c (red dots).

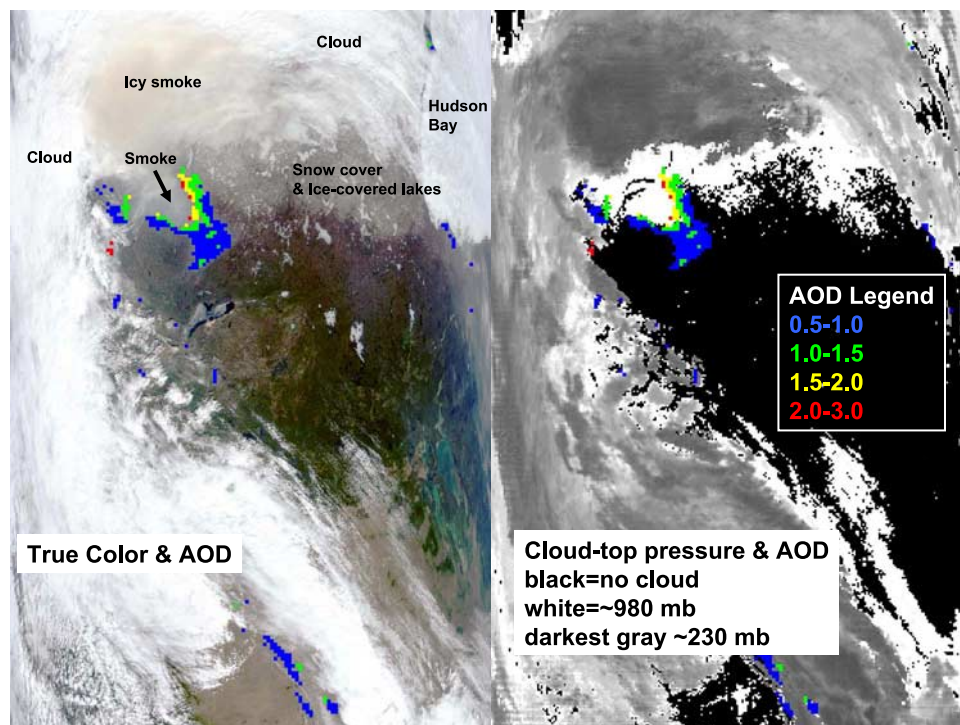


Figure 7. Composite of MODIS (left) true-color and level 2 AOD and (right) level 2 cloud top pressure and AOD. Image date/time is 29 May 2001, 1840 UTC. Features are labeled.

smoke appears thicker at the oblique view angle, thus better areal coverage is obtained and the height retrievals are less sensitive to the underlying cloud deck. The right-side image is a specially generated stereo height product using MISR’s 46° and 60° forward pointing cameras. The southern portion of the smoke cloud is at an altitude of about 3.5 km; however, the smoke further to the north is at heights of about 12–13 km above mean sea level (amsl). The height fields pictured here are uncorrected for wind effects; wind-corrected heights (which have higher accuracy but sparser spatial coverage) for this smoke pall are about 0.5 km higher.

[29] Figure 9 shows a “profile” of MISR stereo height from the scene in Figure 8. This is simply a frequency distribution of the heights, and we focus on the local maxima. From these we conclude that there are primarily three cloud or plume decks in the MISR scene. By subsetting the stereo height image we can identify the distinct compositions to the three decks. The lowest deck, at ~3.2 km amsl, is the tongue of smoke in the southern portion of the MISR scene. The water-ice cloud deck is mostly between 6.5 and 8.0 km. The high smoke is grouped at 12.0 km, 2–3 km above the tropopause, which here is determined from the 1200 UTC 29 May radiosonde from Fort Smith, NT (not shown). The MISR stereo height retrievals of the “day-after” Chisholm plume are the first independent, objective assessments of the initial stratospheric injection potential of a pyroCb.

3.2.6. TOMS AI

[30] Next we introduce level 2 TOMS AI (Figure 10). Each pixel is mapped at its effective resolution taking into account the TOMS scan pattern. The time of these measurements is ~1800 UTC, about 45 min earlier than the Terra overpass, thus sampling approximately the same scene as

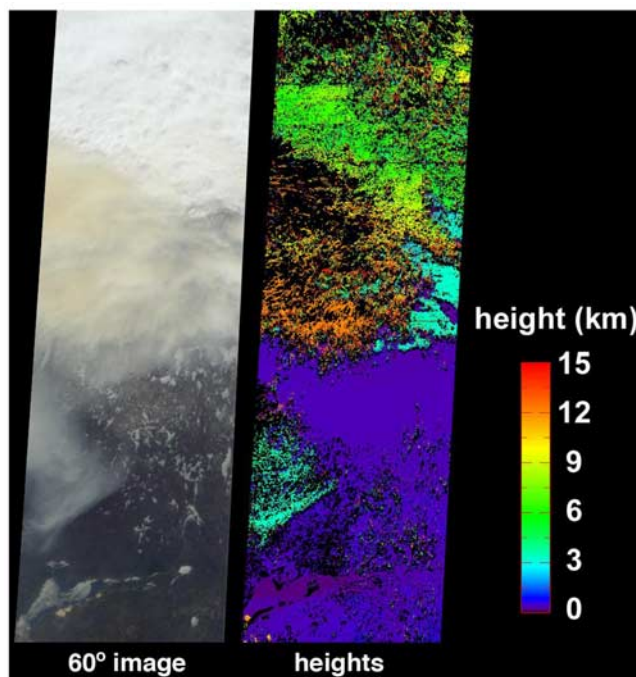


Figure 8. MISR true-color and stereo heights of 1840 UTC 29 May 2001 Chisholm plume and meteorological cloud to the northeast. The true-color image is from the 60° forward camera. The stereo heights are a special retrieval using MISR’s 46° and 60° forward pointing cameras.

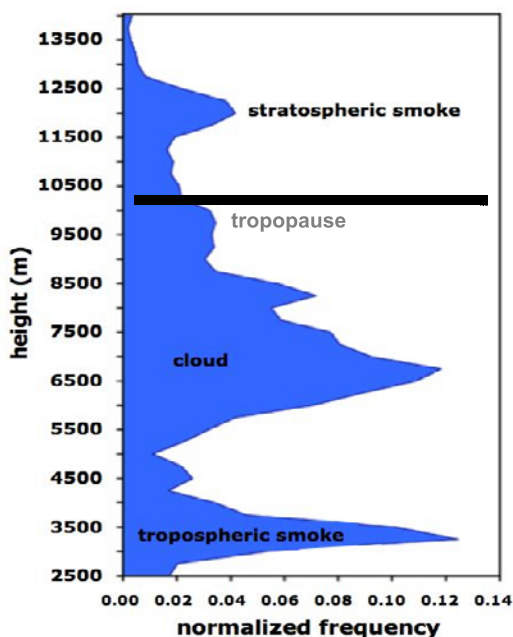


Figure 9. “Profile” of MISR stereo heights. This is a stereo height frequency distribution. Local maxima and the cloud/plume subscenes which they represent are labeled. Tropopause height from Fort Smith (60°N, 110°W) radio-sonde is marked by the horizontal bar.

Terra. The peak AI is 31.2 in the core of the smoke plume, roughly where the MODIS color of the smoke is intense brown. In the version 7 result reported by FS03, the plume core AI had an artificial limit of 12.8, thus we see an

immediate advantage to the version 8 AI retrieval. In our investigation of level 2 AI for other thick and deep smoke plumes (which includes published cases cited in section 1 and several other works in progress), the peak value of 31.2 is unrivaled. Although the aerosol index is ultimately a qualitative indicator, the relevance of values in the 20s and 30s is evident in the context of the MODIS smoke color, low brightness temperature, and MISR stereo heights: they signify a plume with particularly high absorption optical depth and high altitude aerosols. Next we attempt to explore these relations more exhaustively.

3.3. Plume and Cloud Height

[31] The combination of satellites viewing the 29 May Chisholm day-after plume allows us to obtain greater insights into the cloud/plume complex. We choose 65°N for a slice through the core of the smoke. In Figures 11 and 12 we show MISR, MODIS, and TOMS data within $\pm 2^\circ$ latitude, from 125° to 95°W, which spans the smoke pall and continues through a solid deck of pure water-ice clouds to the east and west. In Figures 11 and 12 we plot individual pixel values and a solid line, a boxcar average chosen to discern a general pattern but preserve small-scale structure.

[32] Figure 11 contains MISR stereo heights and TOMS AI, and an effective opaque cloud top height derived from MODIS THIR BT. Here we use a temperature profile from NCEP Reanalysis for 1200 UTC 29 May interpolated to 65°N, 110°W for the BT-height relation. We see that the entire slice is composed of cloud; that is, BT gives an unbroken stretch of elevated heights, from 3.0 to 10.5 km. Cloud tops estimated in this way are near 5 km amsl at the east and west ends, and rise toward the center longitudes. To assess cloud altitude with respect to the tropopause,

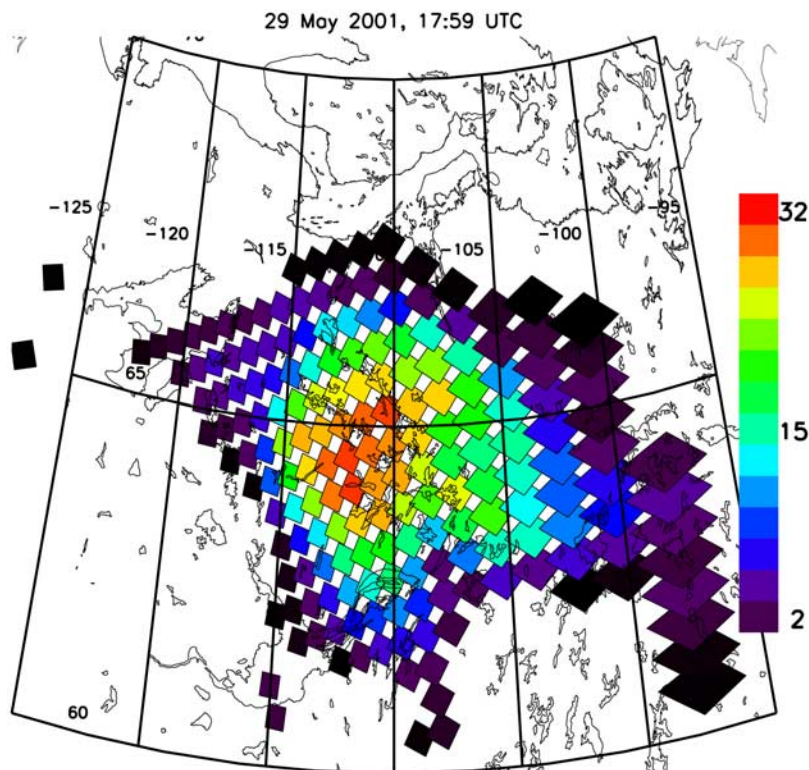


Figure 10. Earth-Probe TOMS level 2 aerosol index at ~ 1800 UTC 29 May 2001.

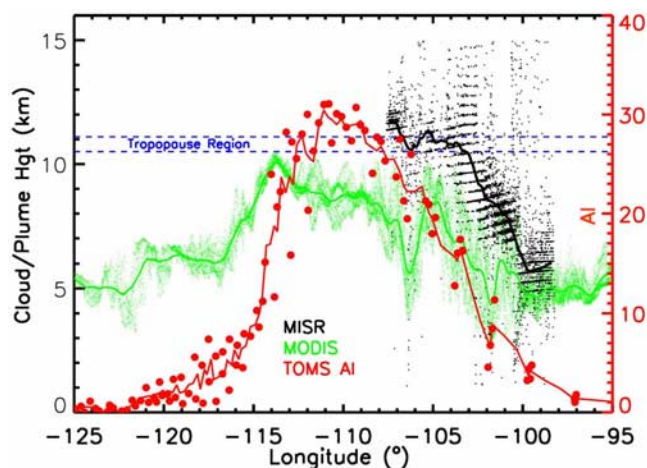


Figure 11. Analysis of MISR stereo heights, TOMS AI, and MODIS IR-inferred cloud tops along the 65°N parallel. All pixels within 2° of 65°N are shown. For details of MODIS BT-to-cloud top altitude determination, see text. Lines through each data item are from boxcar smoothing. For tropopause region determination, see text.

we determine the local tropopause region using two approaches. The top of the tropopause region is the altitude of the temperature minimum, averaged from the radiosonde profiles at Fort Smith (60°N, 110°W) and Cambridge Bay (69°N, 105°W) for each station's two 29 May measurements. This value is 11.1 km. The tropopause height is calculated by the dynamical definition, using potential vorticity equal to 2.5 potential vorticity units, for the 1200 UT 29 May NCEP reanalysis fields. That gives a tropopause height at 65°N, 110°W of 10.5 km. The opaque cloud tops rise to the tropopause at 114°W. Both AI and BT-estimated cloud heights rise toward the center of this slice at 65°N. At the east and west edges, the AI is essentially zero, which means no absorbing aerosol above the surface observed by TOMS. The sharpest gradients of AI are where the MODIS BT-height gradients are also largest, between ~114–116°W and 102–105°W. In the plume core longitudes, where the BT-height is greatest, the correlation with AI breaks down. The peak AI is at ~111°W, about 3° east of the deepest opaque cloud top. Considering the very strong aerosol signal in the MODIS color throughout the core of the plume, the peaking of AI at 111°W may well indicate a local maximum in plume altitude instead of an increase in optical depth. This decoupling of the correlation between THIR BT and AI would occur if the smoke aerosols here were small enough to be transparent to emitted 11 μm radiance. In summary the strong positive correlation between the AI and BT-height gradients approaching the plume core indicates that the plume core AI variation reveals a local maximum in smoke altitude.

[33] We can assess this independently with the MISR stereo heights. Even though the MISR swath does not cover the entire slice in Figure 11, these data offer a distinct advantage over MODIS THIR BT, because the stereo height retrieval does not depend on THIR opacity. Moreover, the MISR swath contains both meteorological cloud and smoke, and covers a portion of the AI swath where values range from marginal to extreme. We see that in the eastern edge of

the MISR swath, where AI is ~ 3 (just above noise levels), the typical MISR stereo height (~ 5.7 km) is relatively close to the BT-height estimate (~ 5 km). Here the dominant reflecting layer is the water-ice cloud deck. But the rapidly “thickening” smoke to the west gives MISR stereo heights that increase more rapidly than the MODIS BT-height estimate. Near the western edge of the MISR swath, where AI is over 20, the MISR-MODIS height difference is between 2 and 5 km. At the western edge the central values of MISR stereo height are above the tropopause and the east-to-west slope is still positive. Here the AI slope is also positive. Thus it appears that the smoke plume to the west of the MISR swath at 65°N continues to increase in height and is mainly in the lowermost stratosphere. It is not possible to resolve the relative contribution of increasing aerosol optical depth and plume altitude for the peaking of AI, but we attempt to address that by invoking MODIS visible data in Figure 12.

[34] In Figure 12 we keep the MISR stereo heights and TOMS AI, but replace MODIS IR data with visible reflectance at the three wavelengths used in the true-color imagery. By plotting these, color coded accordingly, we can infer changes in aerosol optical depth by changes in color with respect to the general whiteness of the water-ice cloud deck that covers the west and east extrema of the slice at 65°N. The white water-ice cloud by definition gives approximately equal reflectances at the three true-color wavelengths. The brown hue of the smoke plume (see Figure 4a) is a result of relatively small reflectance contribution at the short (i.e., blue) wavelength, and dominance of red plus green wavelengths. Total brightness of the scene can be inferred by the “sum” of the three channels' reflectances. On the west and east edges of the scene in Figure 12, where the water-ice cloud deck dominates, the total visible reflectance is large while the red and green reflectances are equal to or even less than the blue-channel reflectance. Toward the center from each direction the blue-channel reflectance diminishes preferentially, first in a transition zone, and bottoms out between 108.5 and 113°W, where there is no discernable change in the intensity of the red + green versus blue reflectance. This may be viewed as a zone where the color-inferred aerosol

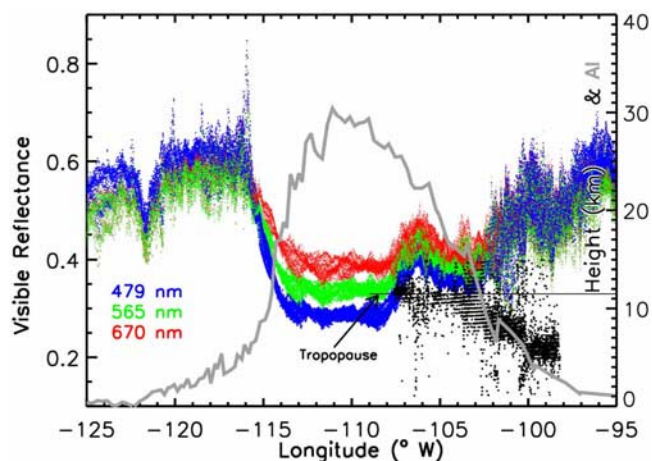


Figure 12. Analysis like in Figure 11 but with MODIS true-color-channel reflectances instead of cloud top. Each color channel is appropriately color coded.

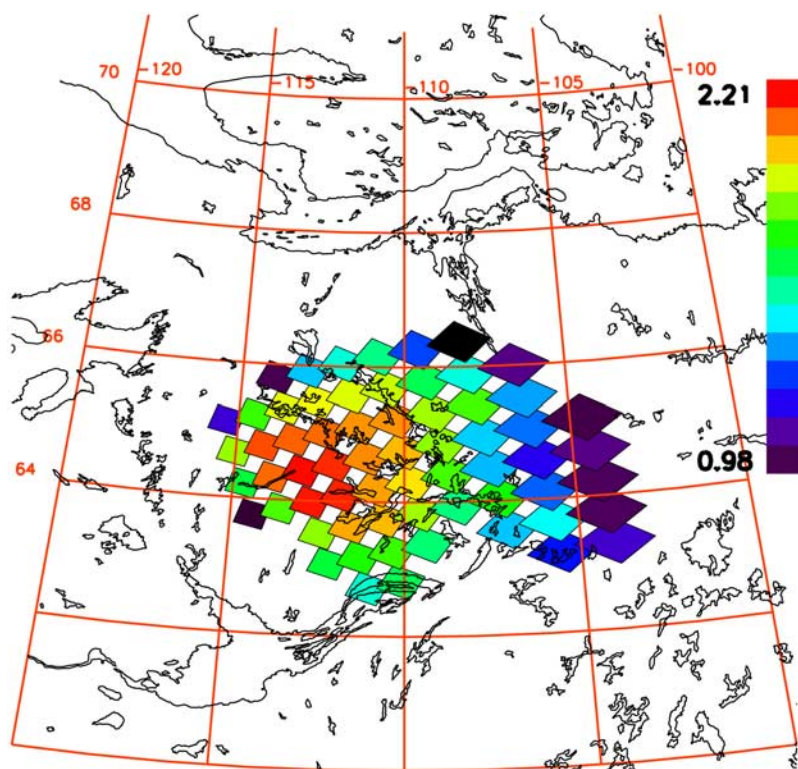


Figure 13. Derived extinction AOD on 29 May 2001 from TOMS AI for pixels with $AI \geq 15$. Single scatter albedo assumed as 0.9. See text for details.

abundance is both large and essentially unchanging. But it is within this zone that the smoothed AI line increases to a peak at 111°W . Considering our earlier interpretation of the increasing AI being strongly driven by plume altitude, this peaking of AI in the zone of thickest, and approximately constant, smoke aerosol suggests increasing plume altitude even above the high west-end MISR values.

3.4. Stratospheric Smoke Mass

[35] We can estimate the mass of smoke injected into the lower stratosphere using inferences gained from the previous analysis. The synthesis of the AI with MODIS and MISR allows us to conclude that the parts of the Chisholm plume with AI greater than a certain threshold are above the tropopause. The analysis of Figures 11 and 12 lead us to use $AI = 15$ for a stratospheric aerosol threshold. For comparison we will also use a larger (i.e., more conservative) threshold of $AI = 19$.

[36] The use of the TOMS near-UV measurements to retrieve aerosol properties over clouds is a challenging enterprise. The cloud-free approach [Torres *et al.*, 1998, 2002b] is not directly applicable here because, in addition to the known dependences of the AI on aerosol microphysical properties and total optical depth, the albedo of the bright reflecting background must also be known. Although the aerosol layer height dependence when the aerosol is above a bright surface is reduced [Torres *et al.*, 1998; de Graaf *et al.*, 2005] the relative cloud-aerosol separation must also be accounted for. However, we can use the heights of the smoke plume and the cloud layer from MISR. In spite of these difficulties we have attempted a quantification effort taking advantage of current ongoing work by one of the

coauthors (O. Torres) toward the development of a retrieval approach of aerosol absorption over clouds. Sensitivity analyses (not shown) indicate that the conversion of AI to extinction optical depth and single scattering albedo by an inversion procedure requires accurate characterization of the reflecting lower boundary. It is possible however, to directly derive an estimate of the aerosol absorption optical depth because the uncertainty attributable to cloud albedo affects the derived extinction optical depth and single scattering albedo in opposite directions. Therefore, a cancellation of errors takes place, and a realistic estimate of the absorption optical depth can be obtained provided that other relevant input (i.e., aerosol particle size distribution, and aerosol layer height) are accurately characterized. We have preliminarily applied this inversion approach to the TOMS observations of Chisholm plume on 29 May. The particle size distribution is based on AERONET observations for biomass burning aerosols [Torres *et al.*, 2002b]. The aerosol layer height derived from MISR observations is assumed in the retrieval. A cloud top at 600 hPa was also assumed. Under these assumptions the distribution of the absorption optical depth was obtained. These results are just an attempt to express the qualitative AI parameter into a more physically meaningful quantity and should be regarded as very preliminary. The derived aerosol absorption optical depth could be off by as much as a factor of two.

[37] We calculate smoke mass using extinction AOD, derived from absorption AOD divided by the co-single-scatter-albedo ($1 - \omega_0$). The extinction AOD for 29 May is shown in Figure 13, where a typical value for forest fire smoke of 0.9 is used for ω_0 [Reid *et al.*, 2005b]. Mass per pixel is then the product of the extinction optical depth,

Table 1. Chisholm Stratospheric Smoke Plume Mass for Two Stratospheric AI Thresholds and Six ω_0 Assumptions^a

ω_0	AI = 15	AI = 19
0.70	1.8	1.4
0.75	2.2	1.7
0.80	2.7	2.2
0.85	3.6	2.8
0.90	5.5	4.2
0.95	10.9	8.3
Mean	4.4	3.4

^aUnit is 10^4 tons.

specific extinction, and pixel area. We assumed a specific extinction mass factor of $5 \text{ m}^2/\text{kg}$ [Reid *et al.*, 2005a]. We will calculate aerosol mass using this assumption and two bounding values for ω_0 , 0.7 and 0.95 to cover a suitable range given for smoke in the literature. Hence the derived extinction AOD will vary by a factor of 1/3 to 2 from those shown in Figure 13.

[38] Integrating the TOMS pixel footprint for the above mentioned AI threshold gives an area range of 1.17×10^5 to $1.69 \times 10^5 \text{ km}^2$ (mean = $1.43 \times 10^5 \text{ km}^2$). The resultant mass of smoke is for the two AI thresholds and three ω_0 is summarized in Table 1. As a point of qualitative comparison, we relate this burden to the integrated Northern Hemispheric stratospheric aerosol burden for near background conditions (1979) calculated by Kent and McCormick [1984]: $\sim 3 \times 10^5 \text{ t}$. The Chisholm pyroCb injected a mass of smoke aerosol equivalent to between 4.6% and 36.3% of the background hemispheric aerosol load. The mean value, for the AI = 15 threshold, is 14.8%.

[39] Now we reconcile the stratospheric smoke injection with the emission from the Chisholm fire during pyroconvection. Area burned during the blowup on 28 May was approximately 50000 ha [Luderer *et al.*, 2006, and refer-

ences therein]. Total particulate matter emitted (TPM) from an area burned is expressed per equation (1)

$$\text{TPM} = \text{Emission factor} \times \text{Fuel load/area} \times \text{Area burned.} \quad (1)$$

[40] Combusted fuel consists of surface and crown matter. For the area burned during the 28 May pyroconvection this is the sum of $\sim 9.0 \text{ kg/m}^2$ for the surface [Alberta Sustainable Resource Development, 2001] and 1.0 kg/m^2 for the crown (B. J. Stocks, personal communication, 2007), giving a fuel consumption of $5 \times 10^6 \text{ t}$. For emission factor we take two values from Reid *et al.* [2005a, Table 6] for temperate/boreal forest, to give a range of emissions (expressed as the ratio of kg emitted to kg consumed): those of Hobbs *et al.* [1996] (.018) and Nance *et al.* [1993] (.029). These bracketing values result in total particulate emissions between $9.0 \times 10^4 \text{ t}$ and $1.45 \times 10^5 \text{ t}$. From Table 1, the stratospheric smoke mass injection from the Chisholm pyroCb was between 0.3% and 2.2% of fuel consumed during pyroconvection. In relation to TPM, the fraction of stratospheric smoke was between 9.6% and 121.0%. The mean, for the AI = 15 threshold, and mean TPM ($1.175 \times 10^5 \text{ t}$), is 37.9%. The simulation of the Chisholm pyroCb by Trentmann *et al.* [2006] resulted in a stratospheric aerosol injection proportion of 8%, near the low end of the range reported here. Obviously the fact that the upper value exceeds 100% suggests that $\omega_0 = 0.95$ is unrealistically large for the Chisholm plume or TPM estimates in this case are too low.

4. Comparison of 29 and 30 May Views

[41] Figure 14 contains the MODIS daytime views of the Chisholm smoke 1 d later, on 30 May (1745 UTC). The

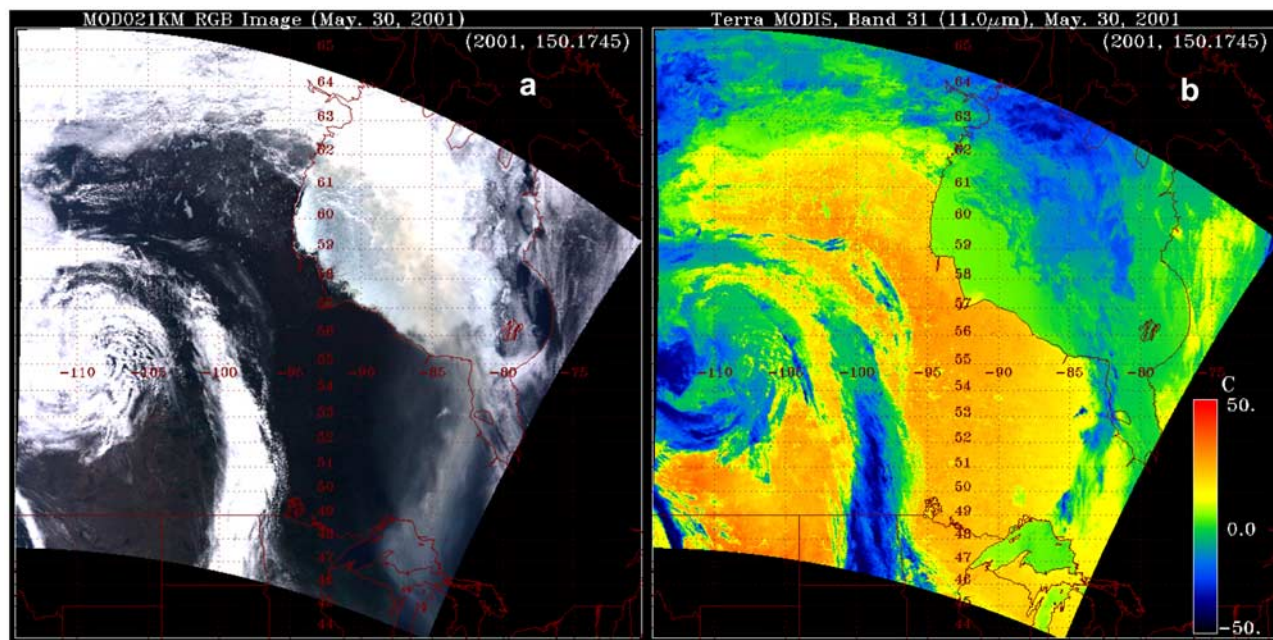


Figure 14. (a) MODIS stretched true-color image for 1745 UTC 30 May 2001. (b) MODIS $11 \mu\text{m}$ BT image for 1745 UTC 30 May 2001.

plume has been stretched and advected under the influence of anticyclonic wind. At this time the plume extends from Northwest Territories, across Hudson Bay and into the Great Lakes and Michigan. UTLS-level wind direction in the Hudson Bay and USA part of the plume is northerly (not shown). According to the true-color image in Figure 14a the smoke is evidently thinner than on 29 May. Skies over land surfaces adjacent to the plume in Canada and the USA are apparently cloud free. Hudson Bay appears to contain widespread ice and some overlying water-ice cloud, detectable through the translucent smoke. The THIR image of Figure 14b reinforces the determination that land areas of the upper Midwest United States and Manitoba are cloud free. Northern Hudson Bay has opaque low and midtropospheric cloudiness. The smoke plume from James Bay to Lake Superior appears to have a residual signal in THIR, indicating that the transition from opaque smoky ice to transparent smoke is not yet complete, ~ 1.5 d after pyroconvection.

[42] TOMS AI map for 30 May is shown in Figure 15a. The times of the Terra and Earth-Probe overpasses coincide within 2 h. Not surprisingly, the same general shape of the MODIS view of the plume is reproduced. However, the AI gives detail that allows us to infer local extrema in plume altitude. There are two local AI maxima. In both areas $AI > 20$, values representative of the core of the 29 May plume. At neither AI maximum is the visible optical thickness (as inferred from Figure 14a) apparently as large as it was on 29 May; thus the local AI extrema may indicate plume altitude extremes. One of the maxima is west of James Bay. Here the plume in the true-color MODIS view is obvious, but portions of the plume south of the AI maximum and north of the Canada/U.S. border are equally optically thick in the visible, and THIR, but do not have such a large AI signal. Thus this and the other AI maximum to the north may identify where the plume protrudes most deeply into the stratosphere.

[43] The two aforementioned AI maxima lag upstream of plume's forward edge over Michigan. Considering our determination that the core of the 29 May plume topped out in the lower stratosphere, hence above jet stream altitude, it is reasonable to conclude that the vertical range of the young Chisholm smoke plume spanned the UTLS; and as it deformed during advection the smoke at jet stream level advanced far beyond (i.e., to Michigan on 30 May) the highest stratospheric smoke over and/or near Hudson Bay.

5. Chisholm Plume's First Week

[44] The evolution of the Chisholm smoke plume for the balance of its first week of existence is captured in the AI maps of Figure 15. As expected, the maximum AI on each day between 31 May and 4 June declines as the plume shears horizontally. The plume snakes into a wave signature on 31 May, crossing the U.S. Atlantic coast and extending to Labrador. Note the reproduction of two localized AI maxima, one in "mid" plume and the other lagging over James Bay. On 1 June, as the plume takes on a complete wave signature between Quebec and just south of Iceland, a distinct AI maximum appears in the "trough" of the wave over the Atlantic near 38°N (again lagging far behind the plume's leading edge). By 2 June the leading portion of the

Chisholm smoke plume passes over the United Kingdom and resides as far eastward as France, while the western portion (including the AI maximum) starts to form into an apparent cyclonic shape over the central Atlantic. On 3 and 4 June the AI pattern breaks up; the downwind (i.e., eastern) edge enters the Mediterranean region while the lagging plume over the central Atlantic appears to swirl and stagnate. In general the persistence of an AI plume for 1 week and the distance between Alberta and the Mediterranean Sea is by itself an indicator of an extremely unusual aerosol perturbation. This perturbation consists of a large abundance of aerosol material and a residence altitude likely from upper tropospheric jet stream levels to several km into the lower stratosphere.

6. Summary

[45] Our aim was to characterize and establish important parameters related to a young stratospheric smoke plume. The case chosen is that of the Chisholm (Alberta) pyroCb of 28 May 2001. This case, now the subject of multiple papers, is an excellent example of the most extreme form of pyroconvection because of the many space- and ground-based observations of the blowup and aftermath. We focused on the immediate aftermath (from hours to 1 week old), which is an important timeframe for regional or global transport/chemistry/cloud process models to consider as initial conditions.

[46] The Chisholm pyroCb (FS03, R07) has now been confirmed to have injected a large quantity of smoke into the lower stratosphere, even above the altitude of the local temperature minimum, as evidenced from satellite imagery less than $1/2$ d after the pyroconvection ended. MISR stereoscopic height retrievals give the first independent, objective, and detailed confirmation of stratospheric smoke in a young pyroCb plume. MODIS true-color and IR imagery, TOMS aerosol index and MISR stereo heights together allowed us to gain advanced insights into these peculiar UTLS pyroCb plumes. For instance, level 2 AI can reveal variations of plume altitude within a broad or optically thick plume.

[47] The Chisholm pyroCb stratospheric plume on the day after injection covered an area of approximately $1.43 \times 10^5 \text{ km}^2$, with a mass estimated at between 1.39×10^4 and $10.89 \times 10^4 \text{ t}$. This represented between 0.3% and 2.2% of the total fuel consumed during pyroconvection. It also represented between 10 and 121% of the total particulate emissions, calling into question typical assumptions for single scatter albedo of forest fire smoke or emissions estimates/assumptions in this case. The stratospheric mass injection also was related to hemispheric sulfate aerosol background burden; estimated to be roughly 15% of hemispheric aerosol by mass.

[48] Several peculiar traits of the Chisholm plume were in evidence in the Earth-viewing satellite data. For instance, the THIR GOES animation of the first day of plume existence showed that the core BT was close to or even colder than the ambient atmosphere's temperature minimum for ~ 13 h after pyroconvection. During that time the BT minimum actually decreased for about 8 h. The plume was obviously smoke dominated as inferred from the brown color in MODIS imagery, but was also distinctly colder than

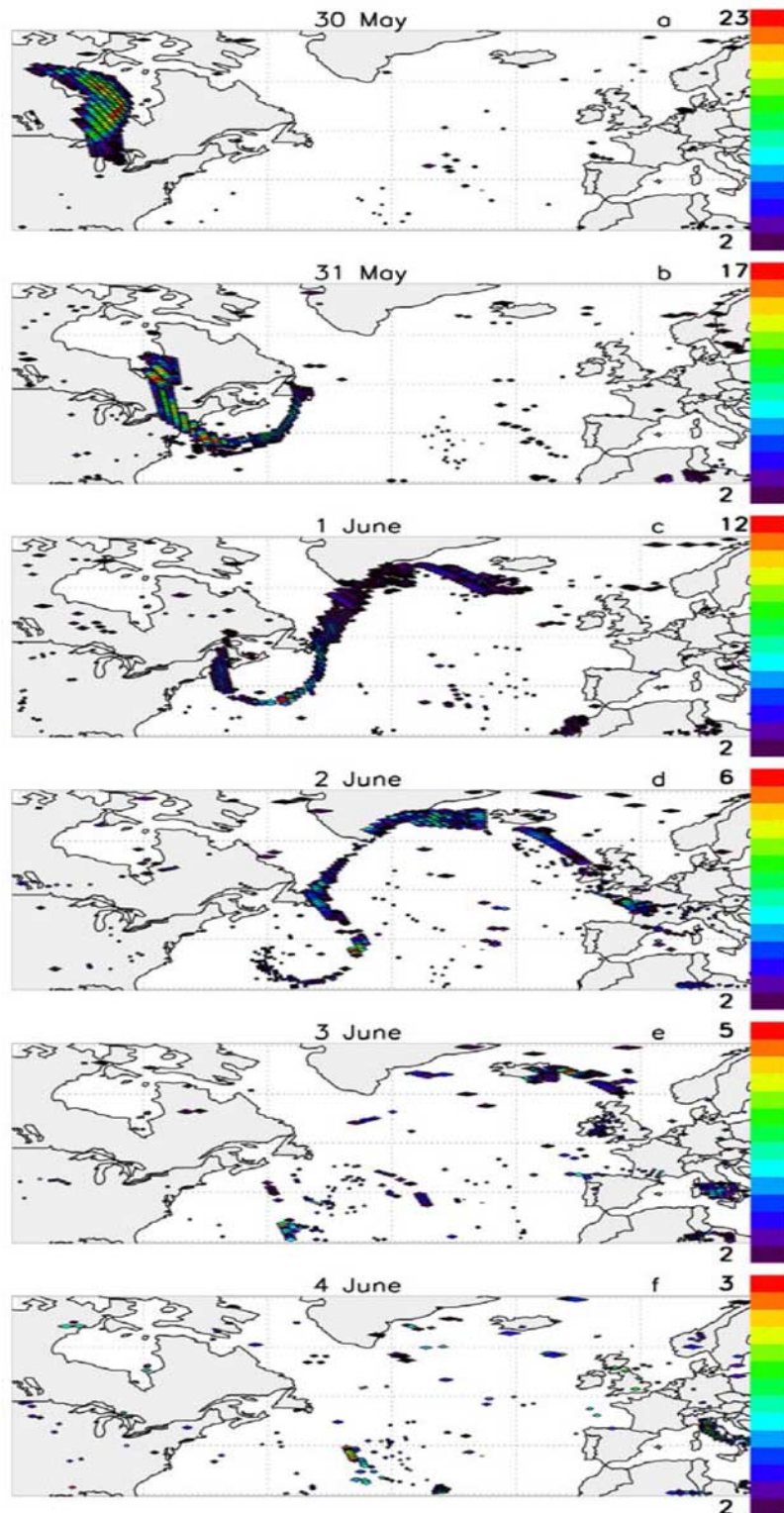


Figure 15. (a) TOMS level 2 AI for 30 May 2001. (b) TOMS level 2 AI for 31 May 2001. (c) TOMS level 2 AI for 1 June 2001. (d) TOMS level 2 AI for 2 June 2001. (e) TOMS level 2 AI for 3 June 2001. (f) TOMS level 2 AI for 4 June 2001. Rainbow color scaling for each panel goes from AI = 2 to the daily maximum.

all neighboring clouds, a combination that confounded both the operational MODIS cloud and aerosol retrieval algorithms. Split-window BTDA analyses were useful in distinguishing the smoke plume from water-ice clouds,

indicating the smoky ice was composed of particles less than half the ice particle effective radius.

[49] Visible reflectance and THIR analysis of the “day-after” Chisholm plume led us to conclude that the

uppermost particles in the young plume were a peculiar mixture of unadulterated dry smoke and smoky ice crystals significantly smaller than normal high cirrus ice crystals. The color of the plume and AI proved that the dominant material in the plume was smoke. This smoky cloud's core was effectively opaque in THIR at the tropopause.

[50] The Chisholm smoke plume "dried out" into transparent (in THIR) smoke in a process that exceeded 1.6 d, a significantly longer sublimation timescale than for normal cumulonimbus cirrus blow off. AI of the aging Chisholm plume was used to locate the maximum stratospheric plume height, which lagged far behind the leading edge. After 1 week the plume's leading edge had snaked as far east as the central Mediterranean; a portion (perhaps the highest smoke) of the plume lagged, stagnated, and circulated over the mid-Atlantic. The companion paper by *Fromm et al.* [2008] presents initial profile measurements of the Chisholm plume there on 5 June and upstream over Quebec (near the tail end of the AI plume) on 1 June.

[51] For the first time, several important initial constraints are placed on an extreme pyroCb event that polluted an entire hemisphere (see the companion paper, *Fromm et al.* [2008]). A single pyroconvective explosion has now been documented from the ground to the stratosphere with metrics that will enable comparisons with other pyroCbs, volcanoes, and conventional aerosol measures for the stratosphere.

[52] **Acknowledgments.** We wish to thank Rong Rong Li for her assistance with the MODIS data and maps. We are also grateful to Bill Rose for his expert insights with respect to the split-window analysis. Fred Prata provided invaluable interpretations of the Chisholm plume's BTD patterns and model curves used in the BTD figures. We are indebted to three reviewers who gave this paper a thorough and thoughtful critique. M.D.F. and E.P.S. were supported in part by a grant from the NASA Office of Earth Science and in part by NRL internal funding (from the Office of Naval Research). The views, opinions, and findings in this report are those of the authors, and should not be construed as an official NOAA and or U.S. Government position, policy, or decision.

References

- Alberta Sustainable Resource Development (2001), Final Documentation Report, Chisholm Fire (LWF-063), For. Prot. Div., Edmonton, Alberta, Canada.
- Bhartia, P. K. (2007), Total Ozone from backscattered ultraviolet measurements, in *Observing Systems for Atmospheric Composition*, edited by G. Visconti et al., pp. 48–63, Springer, New York.
- Damoah, R., N. Spichtinger, R. Servranckx, M. Fromm, E. Eloranta, I. Razenkov, P. James, M. Shulski, C. Forster, and A. Stohl (2006), A case study of pyro-convection using transport model and remote sensing data, *Atmos. Chem. Phys.*, *6*, 173–185.
- de Graaf, M., P. Stammes, O. Torres, and R. B. A. Koelemeijer (2005), Absorbing Aerosol Index: Sensitivity analysis, application to GOME and comparison with TOMS, *J. Geophys. Res.*, *110*, D01201, doi:10.1029/2004JD005178.
- Diner, D. J., et al. (1998), Multi-angle Imaging Spectroradiometer (MISR) description and experiment overview, *IEEE Trans. Geosci. Remote Sens.*, *36*(4), 1072–1087.
- Fromm, M. D., and R. Servranckx (2003), Transport of forest fire smoke above the tropopause by supercell convection, *Geophys. Res. Lett.*, *30*(10), 1542, doi:10.1029/2002GL016820.
- Fromm, M., J. Alfred, K. Hoppel, J. Hornstein, R. Bevilacqua, E. Shettle, R. Servranckx, Z. Li, and B. Stocks (2000), Observations of boreal forest fire smoke in the stratosphere by POAM III, SAGE II, and lidar in 1998, *Geophys. Res. Lett.*, *27*, 1407–1410.
- Fromm, M., R. Bevilacqua, R. Servranckx, J. Rosen, J. P. Thayer, J. Herman, and D. Larko (2005), Pyro-cumulonimbus injection of smoke to the stratosphere: Observations and impact of a super blowup in northwestern Canada on 3–4 August 1998, *J. Geophys. Res.*, *110*, D08205, doi:10.1029/2004JD005350.
- Fromm, M., A. Tupper, D. Rosenfeld, R. Servranckx, and R. McRae (2006), Violent pyro-convective storm devastates Australia's capital and pollutes the stratosphere, *Geophys. Res. Lett.*, *33*, L05815, doi:10.1029/2005GL025161.
- Fromm, M., et al. (2008), Stratospheric impact of the Chisholm pyro-cumulonimbus eruption: 2. Vertical profile perspective, *J. Geophys. Res.*, doi:10.1029/2007JD009147, in press.
- Gothe, M., and H. Grassl (1993), Satellite remote sensing of the optical depth and mean crystal size of thin cirrus clouds and contrails, *Theor. Appl. Climatol.*, *48*, 101–113.
- Guo, S., W. Rose, G. Bluth, and I. M. Watson (2004), Particles in the great Pinatubo volcanic cloud of June 1991: The role of ice, *Geochem. Geophys. Geosyst.*, *5*, Q05003, doi:10.1029/2003GC000655.
- Herman, J. R., P. K. Bhartia, O. Torres, C. Hsu, C. Sefstor, and E. Celarier (1997), Global distribution of UV-absorbing aerosols from Nimbus-7/TOMS data, *J. Geophys. Res.*, *102*, 16,911–16,922.
- Hobbs, P., J. Reid, J. Herring, J. Nance, R. Weiss, J. Ross, D. Hegg, R. Ottmar, and C. Liousse (1996), Particle and trace-gas measurements in smoke from prescribed burns of forest products in the Pacific Northwest, in *Biomass Burning and Global Change*, vol. 1, edited by J. S. Levine, pp. 697–715, MIT Press, Cambridge, Mass.
- Horváth, Á., and R. Davies (2001), Simultaneous retrieval of cloud motion and height from polar-orbiter multiangle measurements, *Geophys. Res. Lett.*, *28*, 2915–2918.
- Jost, H., et al. (2004), In-situ observations of mid-latitude forest fire plumes deep in the stratosphere, *Geophys. Res. Lett.*, *31*, L11101, doi:10.1029/2003GL019253.
- Jovanovic, V. M., M. A. Bull, M. M. Smyth, and J. Zong (2002), MISR in-flight camera geometric model calibration and georectification performance, *IEEE Trans. Geosci. Remote Sens.*, *40*, 1512–1519.
- Jovanovic, V., C. Moroney, and D. Nelson (2007), Multiangle geometric processing for globally geo-located and co-registered MISR image data, *Remote Sens. Environ.*, *107*, 22–32.
- Kaufman, Y. J., D. Tanré, L. A. Remer, E. F. Vermote, A. Chu, and B. N. Holben (1997), Operational remote sensing of tropospheric aerosol over land from EOS moderate resolution imaging spectroradiometer, *J. Geophys. Res.*, *102*, 17,051–17,068.
- Kent, G., and M. McCormick (1984), SAGE and SAM II measurements of global stratospheric aerosol optical depth and mass loading, *J. Geophys. Res.*, *89*(D4), 5303–5314.
- King, M. D., Y. J. Kaufman, W. P. Menzel, and D. Tanré (1992), Remote sensing of cloud, aerosol, and water vapor properties from the Moderate Resolution Imaging Spectrometer (MODIS), *IEEE Trans. Geosci. Remote Sens.*, *30*, 1–27.
- King, M. D., W. P. Menzel, Y. J. Kaufman, D. Tanré, B. C. Gao, S. Platnick, S. A. Ackerman, L. A. Remer, R. Pincus, and P. A. Hubanks (2003), Cloud and aerosol properties, precipitable water, and profiles of temperature and humidity from MODIS, *IEEE Trans. Geosci. Remote Sens.*, *41*, 442–458.
- Livesey, N., M. Fromm, J. Waters, G. Manney, M. Santee, and W. Read (2004), Enhancements in lower stratospheric CH₃CN observed by UARS MLS following boreal forest fires, *J. Geophys. Res.*, *109*, D06308, doi:10.1029/2003JD004055.
- Luderer, G., J. Trentmann, T. Winterrath, C. Textor, M. Herzog, H. F. Graf, and M. O. Andreae (2006), Modeling of biomass smoke injection into the lower stratosphere by a large forest fire (part II): Sensitivity studies, *Atmos. Chem. Phys.*, *6*, 5261–5277.
- Marchand, R. T., T. P. Ackerman, and C. Moroney (2007), An assessment of Multiangle Imaging Spectroradiometer (MISR) stereo-derived cloud top heights and cloud top winds using ground-based radar, lidar, and microwave radiometers, *J. Geophys. Res.*, *112*, D06204, doi:10.1029/2006JD007091.
- Moroney, C., R. Davies, and J.-P. Muller (2002), Operational retrieval of cloud-top heights using MISR data, *IEEE Trans. Geosci. Remote Sens.*, *40*, 15–41.
- Muller, J.-P., A. Mandanayake, C. Moroney, R. Davies, D. J. Diner, and S. Paradise (2002), MISR stereoscopic image matchers: Techniques and results, *IEEE Trans. Geosci. Remote Sens.*, *40*, 1547–1559.
- Nance, J., P. Hobbs, L. Radke, and D. Ward (1993), Airborne measurements of gases and particles from an Alaskan wildfire, *J. Geophys. Res.*, *98*, 14,873–14,882.
- Naud, C., J. Muller, and E. E. Clothiaux (2002), Comparison of cloud top heights derived from MISR stereo and MODIS CO₂-slicing, *Geophys. Res. Lett.*, *29*(16), 1795, doi:10.1029/2002GL015460.
- Naud, C., J.-P. Muller, M. Haeffelin, Y. Morille, and A. Delaval (2004), Assessment of MISR and MODIS cloud top heights through inter-comparison with a back-scattering lidar at SARTA, *Geophys. Res. Lett.*, *31*, L04114, doi:10.1029/2003GL018976.
- Naud, C. M., J. P. Muller, E. C. Slack, C. L. Wrench, and E. E. Clothiaux (2005a), Assessment of the performance of the Chilbolton 3-GHz advanced meteorological radar for cloud-top-height retrieval, *J. Appl. Meteorol.*, *44*, 866–877.

- Naud, C. M., J.-P. Muller, E. E. Clothiaux, B. A. Baum, and W. P. Menzel (2005b), Intercomparison of multiple years of MODIS, MISR and radar cloud-top heights, *Ann. Geophys.*, *23*, 1–10.
- Penndorf, R. (1953), On the phenomenon of the colored sun, especially the “blue” sun of September 1950, *AFCRC Tech. Rep. 53-7*, 41 pp., Air Force Cambridge Res. Cent., Cambridge, Mass.
- Prata, A. J. (1989), Infrared radiative transfer calculations for volcanic ash clouds, *Geophys. Res. Lett.*, *16*(11), 1293–1296.
- Prata, A. J., and I. J. Barton (1993), A multichannel, multiangle method for the determination of infrared optical depth of semitransparent high cloud from an orbiting satellite. Part I: Formulation and simulation, *J. Appl. Meteorol.*, *32*(7), 1623–1637.
- Prata, A. J., and I. F. Grant (2001), Retrieval of microphysical and morphological properties of volcanic ash plumes from satellite data: Application to Mt. Ruapehu, New Zealand, *Q. J. R. Meteorol. Soc.*, *127*(576B), 2153–2179.
- Reid, J., R. Koppmann, T. Eck, and D. Eleuterio (2005a), A review of biomass burning emissions part II: Intensive physical properties of biomass burning particles, *Atmos. Chem. Phys.*, *5*, 799–825.
- Reid, J., T. Eck, S. Christopher, R. Koppmann, O. Dubovik, D. Eleuterio, B. Holben, E. Reid, and J. Zhang (2005b), A review of biomass burning emissions part III: Intensive optical properties of biomass burning particles, *Atmos. Chem. Phys.*, *5*, 827–849.
- Remer, L. A., et al. (2005), The MODIS aerosol algorithm, products and validation, *J. Atmos. Sci.*, *62*, 947–973.
- Rose, W., D. Delene, D. Schneider, G. Bluth, A. Krueger, I. Sprod, C. McKee, H. Davies, and G. Ernst (1995), Ice in the 1994 Rabaul eruption cloud: Implications for volcano hazard and atmospheric effects, *Nature*, *375*, 477–479.
- Rose, W., et al. (2003), The February–March 2000 eruption of Hekla, Iceland from a satellite perspective, in *Volcanism and the Earth's Atmosphere*, *Geophys. Monogr. Ser.*, vol. 139, edited by A. Robock and C. Oppenheimer, pp. 107–132, AGU, Washington, D. C.
- Rosenfeld, D., M. Fromm, J. Trentmann, G. Luderer, M. Andreae, and R. Servranckx (2007), The Chisholm firestorm: observed microstructure, precipitation, and lightning activity of a pyro-cumulonimbus, *Atmos. Chem. Phys.*, *7*, 645–659.
- Siebert, J., C. Timmis, G. Vaughan, and K. Fricke (2000), A strange cloud in the Arctic summer 1998 above Esrange (68N), Sweden, *Ann. Geophys.*, *18*, 505–509.
- Stenchikov, G., M. Fromm, and E. Shettle (2006), Study of long-range transport and stratosphere-troposphere exchange in smoke plumes from forest fires caused by aerosol solar heating, *Eos Trans. AGU*, *87*(52), Fall Meet. Suppl., Abstract A43A-0114.
- Torres, O., P. K. Bhartia, J. R. Herman, Z. Ahmad, and J. Gleason (1998), Derivation of aerosol properties from satellite measurements of backscattered ultraviolet radiation: Theoretical basis, *J. Geophys. Res.*, *103*(D14), 17,099–17,110. (Correction, *J. Geophys. Res.*, *103*(D18), 23,321–23,332, 1998.)
- Torres, O., P. K. Bhartia, J. R. Herman, A. Sinyuk, P. Ginoux, and B. Holben (2002a), A long-term record of aerosol optical depth from TOMS observations and comparison to AERONET measurements, *J. Atmos. Sci.*, *59*(3), 398–413.
- Torres, O., R. Decae, J. P. Veefkind, and G. de Leeuw (2002b), OMI aerosol retrieval algorithm, in *OMI Algorithm Theoretical Basis Document: Clouds, Aerosols, and Surface UV Irradiance*, *OMI-ATBD-03*, vol. 3, version 2, edited by P. Stammes, NASA Goddard Space Flight Cent., Greenbelt, Md. (Available at http://eosps.gsf.nasa.gov/eos_homepage/for_scientists/atbd/docs/OMI/ATBD-OMI-03.pdf)
- Trentmann, J., G. Luderer, T. Winterrath, M. D. Fromm, R. Servranckx, C. Textor, M. Herzog, H.-F. Graf, and M. O. Andreae (2006), Modeling of biomass smoke injection into the lower stratosphere by a large forest fire (part I): Reference simulation, *Atmos. Chem. Phys.*, *6*, 5247–5260.
- Tupper, A., J. S. Oswalt, and D. Rosenfeld (2005), Satellite and radar analysis of the volcanic-cumulonimbus at Mount Pinatubo, Philippines, 1991, *J. Geophys. Res.*, *110*, D09204, doi:10.1029/2004JD005499.
- Waibel, A. E., H. Fischer, F. G. Wienhold, P. C. Siegmund, B. Lee, J. Ström, J. Lelieveld, and P. J. Crutzen (1999), Highly elevated carbon monoxide concentrations in the upper troposphere and lowermost stratosphere at northern midlatitudes during the STREAM II summer campaign in 1994, *Chemosphere Global Change Sci.*, *1*, 233–248.
- Wallace, J., and P. Hobbs (1977), *Atmospheric Science: An Introductory Survey*, Elsevier, New York.
- Wen, S., and W. Rose (1994), Retrieval of sizes and total masses of particles in volcanic clouds using AVHRR bands 4 and 5, *J. Geophys. Res.*, *99*, 5421–5431.
- Yamanouchi, T., K. Suzuki, and S. Kawaguchi (1987), Detection of clouds in Antarctica from infrared multispectral data of AVHRR, *J. Meteorol. Soc.*, *65*, 949–961.
- Yang, P., L. Zhang, G. Hong, S. L. Nasiri, B. A. Baum, H. L. Huang, M. D. King, and S. Platnick (2007), Differences between collection 4 and 5 MODIS ice cloud optical/microphysical products and their impact on radiative forcing simulations, *IEEE Trans. Geosci. Remote Sens.*, *45*, 2886–2899.
- Zong, J., R. Davies, J.-P. Muller, and D. J. Diner (2002), Photogrammetric retrieval of cloud advection and top height from the Multi-angle Imaging SpectroRadiometer (MISR), *Photogramm. Eng. Remote Sens.*, *68*, 821–829.

D. Diner, Jet Propulsion Laboratory, Pasadena, CA 91109, USA.

M. Fromm and E. P. Shettle, Naval Research Laboratory, Washington, DC 20375, USA. (mike.fromm@nrl.navy.mil)

Z. Li, Earth System Science Interdisciplinary Center, University of Maryland, College Park, MD 20742, USA.

D. Lindsey, Regional and Mesoscale Meteorology Branch, National Environmental Satellite, Data, and Information Service, NOAA, Fort Collins, CO 80523, USA.

R. Servranckx, Canadian Meteorological Center, Dorval, QC, Canada H9P 1J3.

O. Torres, NASA Goddard Space Flight Center, Greenbelt, MD 20771, USA.

B. Vant Hull, Cooperative Remote Sensing Science and Technology Center, NOAA, City College of New York, NY 10031, USA.